This is a repository copy of *Emergent magnetism at transition-metal–nanocarbon interfaces*.

Emergent Magnetism at Transition Metal-Nanocarbon Interfaces

F. Al Ma'Mari[a,b], M. Rogers[a], S. Alghamdi[a], T. Moorsom[a], S. Lee[c], T. Prokscha[d], H. Luetkens[d], M. Valvidares[e], G. Teobaldi[f,g], M. Flokstra[c], R. Stewart[c], P. Gargiani[e], M. Ali[a], G. Burnell[a], B.J. Hickey[a] and O. Cespedes[a,1]

[a]*School of Physics and Astronomy, University of Leeds, Leeds LS2 9JT, UK.;* [b]*Department of Physics, Sultan Qaboos University, P.O. Box 36, 123 Muscat, Oman;* [c]*School of Physics and Astronomy, SUPA, University of St Andrews, St Andrews KY16 9SS, UK;* [d]*Laboratory for Muon Spin Spectroscopy, Paul Scherrer Institut, 5232 Villigen, Switzerland;* [e]*ALBA Synchrotron Light Source, E-08290 Barcelona, Spain;* [f]*Stephenson Institute for Renewable Energy, Department of Chemistry, University of Liverpool, Liverpool L69 3BX;* [g]*Beijin Computational Science Research Centre, Beijing 100193 China.*

[1]*Corresponding author email address: o.cespedes@leeds.ac.uk*

Charge transfer at metallo-molecular interfaces may be used to design multifunctional hybrids with an emergent magnetization that may offer an eco-friendly and tunable alternative to conventional magnets and devices. Here, we investigate the origin of the magnetism arising at these interfaces by using different techniques to probe 3d and 5d metal films such as Sc, Mn, Cu and Pt in contact with fullerenes and RF sputtered carbon layers. These systems exhibit small anisotropy and coercivity together with a high Curie point. Low energy muon spin spectroscopy in Cu and Sc-C_{60} multilayers show a quick spin depolarization and oscillations attributed to non-uniform local magnetic fields close to the metallo-carbon interface. The hybridization state of the carbon layers plays a crucial role, and we observe an increased magnetization as sp^3 orbitals are annealed into sp^2–π graphitic states in sputtered carbon/copper multilayers. X-ray magnetic circular dichroism (XMCD) measurements at the carbon K-edge of C_{60} layers in contact with Sc films show spin polarization in the lowest unoccupied molecular orbital (LUMO) and higher π^* molecular levels, while the dichroism in the σ^* resonances is small or non-existent. These results support the idea of an interaction mediated via charge transfer from the metal and dz-π hybridization. Thin film carbon-based magnets may allow for the manipulation of spin ordering

at metallic surfaces using electro-optical signals, with potential applications in computing, sensors and other multifunctional magnetic devices.

Interfaces are critical in quantum physics, and therefore we must explore the potential for designer hybrid materials that profit from promising combinatory effects. In particular, the fine tuning of spin polarization at metallo-organic interfaces opens a realm of possibilities; from the direct applications in molecular spintronics and thin film magnetism to biomedical imaging or quantum computing. This interaction at the surface can control the spin polarization in magnetic field sensors, generate a magnetization spin filtering effects in non-magnetic electrodes or even give rise to a spontaneous spin ordering in non-magnetic elements such as diamagnetic copper and paramagnetic manganese.(1-11)

The impact of carbon-based molecules on adjacent ferromagnets is not limited to spin filtering and electronic transport, but extend to induced changes in the metal anisotropy, magnetization, coercivity and bias.(12-14) Charge transfer and d(metal)-π(carbon) orbital coupling at the interface may change the density of states, spin population and exchange of metallo-carbon interfaces.(4, 15, 16) The interaction between the molecule and the metal depends strongly on the morphology and specific molecular geometry.(17, 18) It may lead to a change in the density of states at the Fermi energy $N(E_F)$ and/or the exchange-correlation integral (I_s) as described by the Stoner criterion for ferromagnetism.(19, 20) The coupling can even extend through a non-magnetic metallic layer that carries the exchange information from a ferromagnetic substrate to an organic layer.(21)

The emergent magnetism measured in Cu/ and Mn/C_{60} multilayers extends as well to other transition metals close to complying with the Stoner criterion such as Sc and Pt –see table 1. We grow our films via DC or RF sputtering and in-situ thermal evaporation (SI Appendix, section 1). Although we could expect that metals closer to the Stoner criterion would present higher magnetization, it is apparent that the magnetic properties of the sample are strongly determined by the charge transfer and coupling between the carbon molecules and the metal. This is the case of Sc as compared to Cu; although Sc is

very close to fulfilling the condition for ferromagnetism, it is also a material very prone to oxidation. Furthermore, the Fermi energy and the structure of Sc are not particularly well matched to those of C_{60}. Copper, on the other hand, has a good d_z-π coupling, close lattice matching and the potential to transfer up to 3 electrons per fullerene cage, and this may result in the higher observed magnetization. The fullerenes may also be replaced by other nanocarbon allotropes with mixed sp^2 and sp^3 hybridization, such as RF-sputtered amorphous carbon (aC) layers. These films have the advantages of being smoother, cheaper than fullerenes and easily compatible with conventional metal sputtering, making them more suitable for potential industrial applications in the future. However, the resulting magnetization as measured using a superconducting quantum interference device -vibrating sample magnetometer (SQUID-VSM; see SI Appendix, Section 1) is on average 20-40% lower than when using C_{60}, although they preserve the same trend observed in C_{60} multilayers, i.e. higher magnetization and coercivity when using copper films.

System	Magnetisation (emu/cc metal)	Coercivity (Oe)
Cu/C_{60}	67±10	90±5
Sc/C_{60}	17±7	75±10
Mn/C_{60}	18±2	75±5
Pt/C_{60}	14±4	65±10
Cu/aC	35±5	95±10
Sc/aC	14±7	75±5

Table 1: Magnetic properties of different nanocarbon hybrids with 2-3 nm thick metal layers and the structure Si(substrate)/Ta(3)/Nanocarbon/Metal/Nanocarbon. All materials are deposited in the same chamber without breaking vacuum and with a base pressure ≤2×10^{-8} mbar. Metals are grown via DC magnetron sputtering, C_{60} is thermally evaporated and amorphous carbon (aC) is RF sputtered from a graphite target.

The magnetization of Cu and Mn – C_{60} multilayers has been measured to be dependent on the metallic film thickness, with a peak at 2-5 nm. However, the magnetic moment in Sc/C_{60} samples is roughly constant. For aC/Cu samples, a factor 2 higher moment is measured between ~2-5 nm, but this difference is not as large as for Cu/C_{60}, where the moment is a factor 6 higher for Cu layers 2-2.5 nm thick than for layers of 3-4 nm. (4) This would be expected if the magnetic contribution is mostly due to the interfacial region, resulting in a surface magnetization of ~0.05 emu/m^2 in C_{60}/Sc and 0.1 emu/m^2 in aC/Cu (see fits in Fig. 1A). The presence of a magnetic moment for films below ~1 nm in Sc/C_{60} seems indicative of a good wetting of the C_{60} by the Sc film, leading to continuous films or large superparamagnetic islands with high susceptibility at room temperature. Copper films grown on C_{60}, on the other hand, tend to form islands that fill the rifts formed on the uneven molecular film (RMS roughness of ~1-2 nm compared to ≲0.5 nm for sputtered metals) before forming a continuous layer. The effect of the metal film thickness in the total roughness of the hybrid multilayer is also related to the formation of clusters. As seen in figure 1B, samples with thin metal layers are smoother than equivalent samples with thick metal layers, which may have an impact on the magnetization.

Pt and Sc-C_{60} samples result in a relatively weak magnetization and low coercivity Hc. According to the Stoner-Wohlfarth model,(22, 23) the coercive field in the easy axis, Hc, should be equal to *2K/Ms*, where K is the magnetocrystalline uniaxial anisotropy and *Ms* is the saturation magnetization. For superparamagnetic systems with random crystal orientations, this equation is modified so that Hc drops with temperature till it reaches a zero ideal value for single magnetic domains at the blocking temperature T_B: (24)

$$H_C \approx \frac{K}{M_s}\left[1 - \frac{T}{T_B}\right] \qquad (1)$$

Zero field cooled-field cooled (ZFC-FC) measurements of thin Sc multilayers (<1nm) show a thermal hysteresis not characteristic of ferromagnetic materials, but rather of superparamagnets or spin glasses below their blocking temperature (Fig. 1C).[25] The magnetic anisotropy derived from the fit of the coercive field to equation (1) is very small, $\lesssim$500 J/m^3 –similar to that of permalloy (Fig. 1D). On the other hand, the blocking temperature is very high, some 885 K, corresponding to a grain size of 20 nm ($K \cdot V \approx T_B$). Thicker Sc(2nm)/C$_{60}$ films display shape anisotropy with saturation fields of 5 kOe (10 kOe) at 300 K and 12 kOe (17 kOe) at 2 K for in-plane fields (out of plane), respectively. The sample saturation magnetization at low temperatures is not reached until fields of >10 kOe are applied for both in-plane and out-of-plane measurements. The atomically rough interface may give rise to weakly coupled magnetic moments with random orientation that do not align easily in smaller fields. That can lead to the observed behavior at low temperatures and the zero field cooled/field cooled measurements for ultra-thin films (<2 nm) with enough random dipolar fields.

Density functional theory (DFT) simulations show that the magnetization is more concentrated at the interface for aC/Cu than for C$_{60}$/Cu samples, resulting in a slower decay of the interface magnetic moment with the metal layer thickness (see SI Appendix, Section 2). This effect is linked to a higher magnetic contribution of the carbon layers in the case of aC compared to C$_{60}$ (Figure 1F). Up to 95% of the moment in Cu/C$_{60}$ is computed to be in the metal, with the remaining 5% in the C$_{60}$, but for Cu/aC the moment in the carbon can be as high as 40% of the total. The calculated Stoner product of the exchange integral (Is) with the density of states at the Fermi level (DOS(E$_F$)) is also smaller for aC/Cu than for C$_{60}$/Cu, which agrees with the lower measured magnetization (Figure 1G).
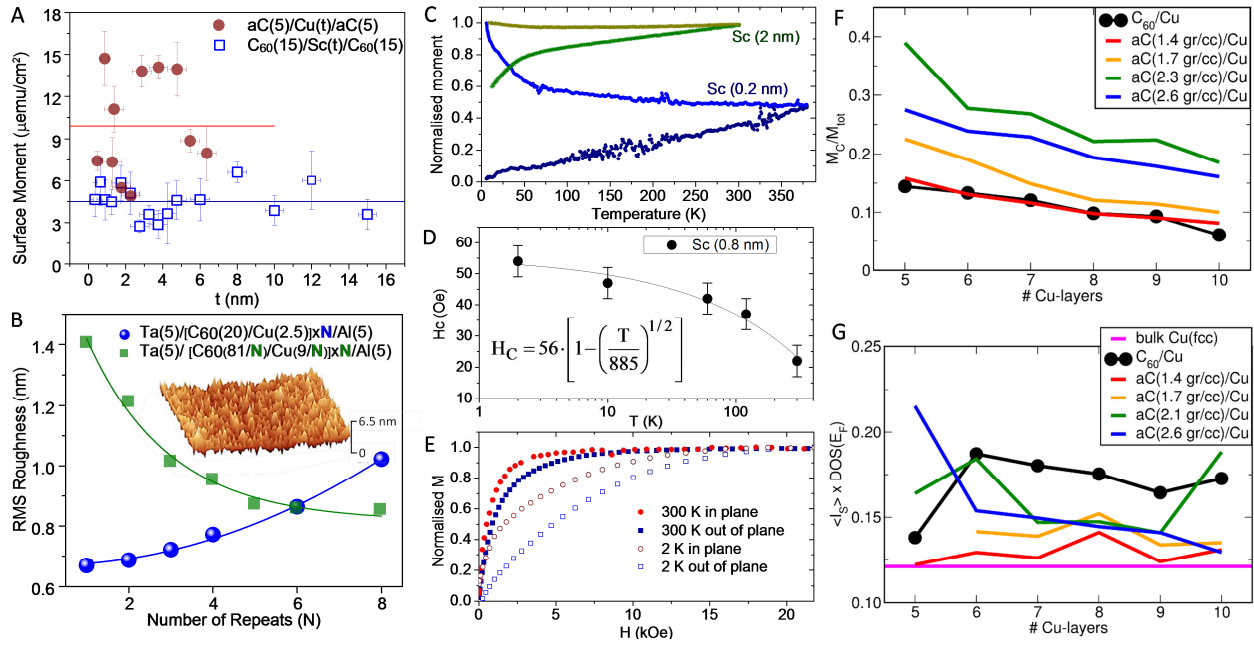
Figure 1: (A) Magnetometry in Si//Ta(3)/C$_{60}$(15)/Sc(t)/C$_{60}$(15)/Al and Si//Ta(3)/aC(5)/Cu(t)/aC(5)/Al multilayers, lines are fit to a constant interfacial magnetic moment. B Sample roughness measured via atomic force microscopy (AFM) vs. number of layers (N) when each film thickness is kept constant (blue dots; line fit to N^2) or when the total multilayer thickness is kept constant (green squares; line fit to asymptotic decay). Both curves should intercept at N=4, but different AFM tips shift them with respect to each other by 1-2 Å. (C) ZFC-FC characteristic measured at 100 Oe for a 0.2 and a 2 nm Sc samples normalized to the low temperature FC moment. The measurement shows thermal hysteresis typical of systems such as superparamagnets and spin glasses. (D) The coercivity of thin Sc films with C$_{60}$ increases upon cooling following the dependence for superparamagnetic systems but with a high blocking temperature of 885 K. (E) C$_{60}$/Sc(2)/C$_{60}$ samples have a high saturation field that increases at low temperatures and with fields perpendicular to the sample. (F) The simulated contribution of the carbon atoms (M$_C$) to the total magnetic moment (M$_{tot}$) for different carbon allotropes and densities shows that the magnetism in the carbon layers is more significant for aC/Cu than for C$_{60}$/Cu. The as-sputtered aC has a density of ~1.7 g/cc, whereas for annealed graphitic films it is ~2.3 g/cc (G) The simulations predict as well a larger Stoner product Is×DOS(E$_F$) for C$_{60}$/Cu than for most aC/Cu systems, in line with the experiments that show larger moments in C$_{60}$-metal samples (Table 1).

In order to investigate the magnetic order at the interface and the propagation length of the effect, we use low energy muon spin rotation (µSR) to provide a magnetic profile of the sample.(26-29) Here, a beam of almost fully polarised positive muons (μ^+) is moderated to keV energies so that their tunable stopping range is of the order of tens to hundreds of nm. The time evolution of the muon spin polarization is a highly sensitive probe of the local magnetism. This is measured through the detection of the anisotropically emitted decay positrons, preferentially emitted along the muon's spin direction at the moment of the decay (see SI Appendix, section 2 for further detail). We use this technique to probe two Sc-C_{60} and Cu-C_{60} samples whose structure includes a thin Sc film of 2 nm (2.5 nm for Cu-C_{60}) and a thick Sc film of 5 nm (15 nm for Cu-C_{60}). Nanoscaling of non-magnetic metals has been shown to give rise to spin ordering.(30-33) The thin films should give rise to a strong magnetic signal, whereas for the thicker films, the interfacial magnetization should be quenched or diluted by the bulk properties of the metal. Full sample structures and muon stopping profiles are shown in figures 2A-B.

The muon spin spectroscopy measurements in Sc-C_{60} and Cu-C_{60} multilayers show similar properties. At 250 K, both samples have an exponential decay of the polarization at zero field and at remanence that may be due to the presence of local magnetic fields with dynamic or topological variations.(34, 35) The amplitude of this signal can be modelled as a function of the contribution of each individual layer in the samples. We find that the C_{60} interfaces with thin metal layers have a much stronger contribution to the depolarization; e.g. for the Sc-C_{60} sample only 2% of the muons stopped in the top C_{60} layer (in contact with Au and thick Sc) contribute to the fast exponential decay vs. 60% of those stopping in the bottom C_{60} layer close to the thin Sc film -see boxes in Figs. 2C-D. Similar fast exponential decay terms can be observed in antiferromagnetic or ferrimagnetic systems with spin canting, which would explain the low remanent magnetization observed in these samples.

The presence of local hyperfine fields may also be evidenced by a zero-field precession signal at 250 K of ~1.1 MHz in Sc/C_{60} and ~0.4 MHz in Cu/C_{60}. Due to the lack of screening electrons in the molecular semiconductor, muons couple with electrons in C_{60} to form the bound state muonium (μ^+-e^-).(36, 37).

Two muonium states are known in C_{60}: i) the exohedral muonium radical with anisotropic hyperfine coupling which is observable below 100 K where the C_{60} rotational modes are frozen, and ii) the endohedral muonium state with a large (vacuum muonium like), isotropic hyperfine coupling. At 250 K the zero-field precession of the exohedral muonium state is not observable due to the fast C_{60} rotation. The isotropic endohedral muonium state should not cause a zero-field precession in the MHz range. However, charge transfer from the transition metal to the C_{60} may cause a deformation of the cage as it is observed for the C_{60} spin triplet state.(38) This deformation may result in a slightly anisotropic hyperfine coupling of the endohedral muonium state which then gives rise to the observed precession frequency in the MHz range, similar as it has been observed in C_{70}.(39)

The difference in the zero-field precession frequencies could then be related to different charge and spin states as a function of the transition metal used as a substrate. The frequencies of oscillation shift in remanence after an applied magnetic field of 300 Oe, and the amplitude of the signal is once again stronger when probing the bottom Sc or Cu/C_{60} interface (Fig. 2E). Fig. 2F (top) shows the change in the precession amplitude attributed to field inhomogeneities. This can be related as well with the random orientation of local dipoles in small fields due to film roughness. The oscillation frequency of the muons in an applied transverse external field of 140 Oe is also increased for implantation energies corresponding to thin Cu layer due to the additional local field (Fig. 2 F-bottom).

Below 100 K, it is possible to observe the zero-field muonium precession frequencies of the exohedral radical state in the range of 1-9 MHz. The fact that the muonium oscillation frequencies are clearly observable implies that the magnetization must be localized close to the Cu layers; otherwise the internal fields would shift/destroy these modes in C_{60}. Their amplitude can be used to probe the magnetic properties of the sample at 20 K (Figs. 2G-H). Given the number of particles implanted in C_{60}, the muonium signal should increase to reach a maxima at 8 keV (Sc-C_{60}) or at 18 keV (Cu-C_{60}). However, the signal remains roughly constant, indicative of magnetic fields perturbing the muonium signal at the higher implantation energies towards the bottom layers.
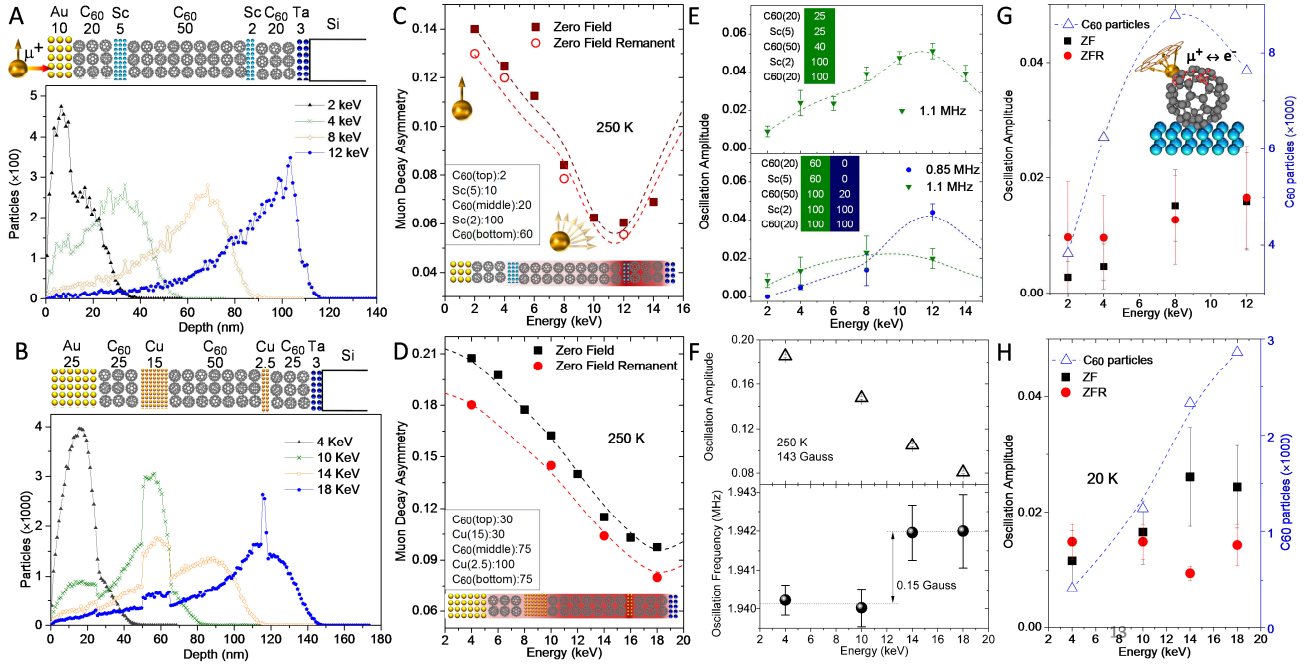
Figure 2: Muon stopping profile for (A) multilayer with the structure Si//Ta(3)/C_{60}(20)/Sc(2)/ C_{60}(50)/Sc(5)/C_{60}(20)/Au(10) (Sc-C_{60}) and (B) multilayer with the structure Si//Ta(3)/C_{60}(25)/Cu(2.5)/ C_{60}(50)/Cu(15)/C_{60}(25)/Au(25) (Cu-C_{60}) –film thickness in brackets in nm. All measurements at 250 K unless otherwise indicated. The amplitude of the slowly relaxing component in the muon precession is reduced as we approach the thin metal films in (C) Sc-C_{60} and (D) Cu-C_{60}, indicating the presence of a depolarization term. Lines are fits to the percentage of muons implanted at each layer contributing to the decay. Schematics show this contribution for each multilayer in a red colour scale. In remanence, the decay is faster but the contributions remain proportionally the same. The magnetic contribution of the bottom metal-C_{60} interfaces leads to a drop of the muon decay asymmetry at 10-12 keV (Sc-C_{60}) or 18 keV (Cu-C_{60}). (E) Top: Muon oscillation amplitude at zero field in Sc-C_{60} (1.1 MHz). Bottom: in remanence with two contributions (1.1 and 0.8 MHz). Lines are a fit to the layers contribution, with the bottom metal and C_{60} layers having the largest input. (F) Oscillation amplitude (top) and frequency (bottom) for the muon precession in Sc-C_{60} with an applied transverse field. Muonium oscillation intensity (1.2, 7.8 and 9 MHz) at 20 K compared to the percentage of muons implanted in C_{60} layers for (G) Sc-C_{60} and (H) Cu-C_{60}. Local magnetic fields at the bottom layers reduce the muonium signal.

The orbital hybridization and molecular coupling with the metal are essential to the charge transfer and emergent magnetism. C_{60} films degrade in ambient conditions due to light induced oxidation, which leads to a decay of the magnetization in a few days if the structures are not protected (Fig. 3A). The concentration of oxygen in C_{60} exposed to atmospheric conditions drops when heated in vacuum at 400 K, reaching near pristine levels by 450 K.[40] The magnetism at Sc/C_{60} interfaces follows this de-oxygenation trend, with increased magnetization after heating to 400-500 K. At higher temperatures, the C_{60} is desorbed from the metallic substrate, leading to a reduced magnetization (Fig. 3B).

For RF sputtered carbon, annealing alters the orbital states, bonding and structure of the layers. We use Raman spectroscopy to track these changes via two vibrational modes: the D band due to the breathing of benzene rings, and the G band due to the stretching of the C-C bond (E_{2g} mode at the Γ-point).[41, 42] As the annealing temperature is increased, the G band shifts to higher frequencies; from 1520 to 1615 cm^{-1}. The intensity of the D band (I_D) with respect to the G band (I_G) gets progressively higher; I_D/I_G increases from ~0.6 in as-deposited films to ~2 after annealing at 875 K for one hour (Fig. 3C). The Raman changes are evidence for the conversion of amorphous carbon into nanocrystalline graphite and the change of orbital hybridization from sp^3 to sp^2.[41-43] In as-deposited films, the estimated percentage of sp^3 orbitals from the I_D/I_G ratio and G peak position is ~15-20%, but at 875 K the percentage has dropped to zero. Above 875 K, graphitic nanocrystals expand until they form full graphite sheets. This leads to the G peak shifting back to lower frequencies and the I_D/I_G ratio decreasing again. In addition to these well characterized changes, above 875 K there is the formation of a new peak at 1275 cm^{-1} that we have labelled as D*. This peak is at a frequency below those conventionally assigned to the D band in graphite for a 532 nm source even in strain/stressed samples (1340-1380 cm^{-1}).[44] This shift could be due to charge transfer and reduction of the carbon atoms.

The structural changes result in a reduced magnetization but increased coercivity (Fig. 3D), with a net enhancement in the B×H energy product (SI Appendix, section 3). These results are reproducible for samples annealed *in-situ* (i.e. heated inside the SQUID at 50 mtorr He atmosphere using an oven probe)

and *ex-situ* (annealed in an external oven under vacuum and then re-measured). The solubility of carbon in solid Cu above 1100 K for 72 h –i.e. at higher temperatures and for longer times than those used in our experiment, is below 5 atomic ppm.(45) Although the solubility of RF sputtered aC in thin films of Cu could be different than in bulk, we do not observe any sign of interdiffusion.
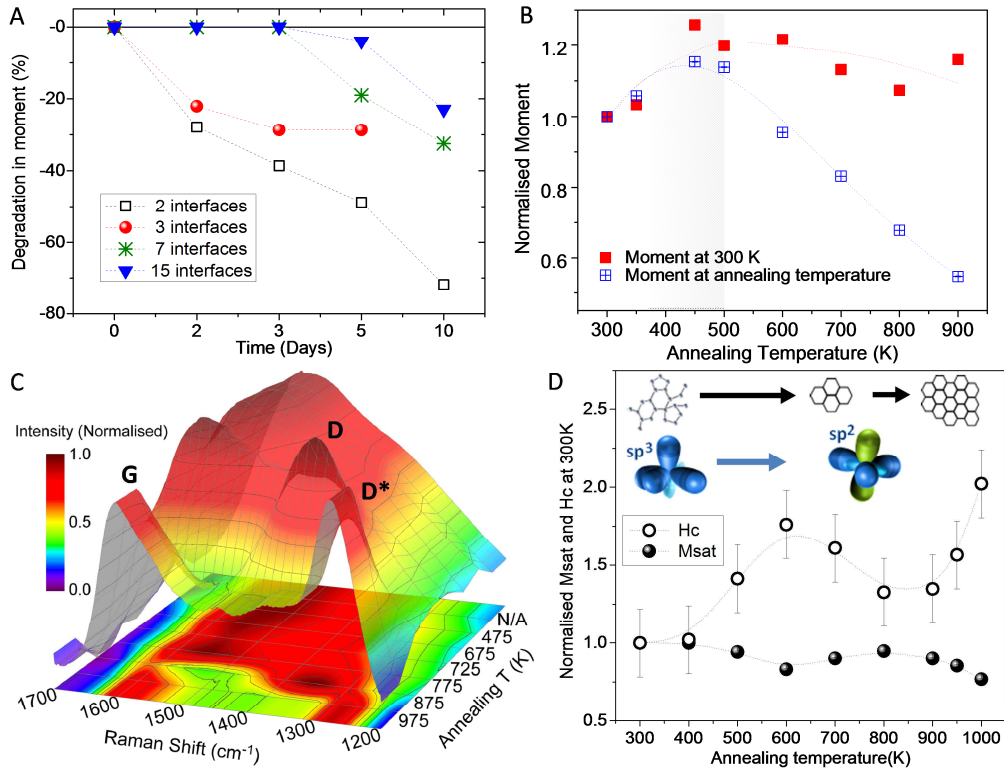

Figure 3: Degradation, annealing and carbon hybridization effects. (A) Time decay of the magnetization in Cu/C$_{60}$ multilayers. In samples with several layers, the bottom interfaces are protected from chemical degradation by the top layers, and the magnetization decay is slow. (B) By annealing, the magnetization of a Si//C$_{60}$(15)/Sc(3nm)/C$_{60}$(15) sample can be enhanced or the degradation compensated. (C) Raman spectra of RF sputtered amorphous carbon on Cu after annealing. At 475-775 K, the G peak moves to higher frequencies and decreases in intensity relative to the D peak. At 875 K and above, the G peak increases again and the D peak has a replica at 1275 cm^{-1}. (D) Evolution of the magnetization and carbon structures during the annealing process. Lines are a guide to the eye. Schematics show the sample structure changes derived from the Raman spectra.

An independent measurement of the magnetization contribution of the carbon material is provided by soft X-ray Absorption Spectroscopy (XAS), exploiting its inherent chemical specificity when the X-ray photon energy is tuned at the carbon K-edge electronic transition. It can therefore be used to assess the presence of magnetic ordering in a given element separately from the contribution of other layers or impurities using X-ray Magnetic Circular Dichroism (XMCD).[46] The K edge XMCD can only probe orbital polarization due to the zero angular momentum of the 1s core shell.[47, 48] In figure 4 we present results in the near edge X-ray fine absorption spectroscopy (NEXAFS) and XMCD at the carbon K-edge of a Sc-C_{60} sample under a 1 T applied magnetic field along the X-ray beam direction, incident at a 45 degree angle on the film. The edge structure of C_{60} on the metal surface is complex, and at room temperature it includes features at 284 (LUMO), 286.2, 286.7 and 287.5 eV (excited LUMO+1, +2, +3) in the π^* antibonding region. [49, 50] The positions of these peaks are lower in energy than for pure C_{60}, which has previously been observed for fullerene films in contact with other conducting magnetic substrates.[51, 52] The σ^* region is above the ionization potential and the modes are less defined, producing wider peaks. The HOMO-LUMO transition (h1u-t1u) in C_{60} is optically forbidden, although it is weakly present via vibrational excitations.

In XMCD spectra at room temperature, the first unoccupied states at the LUMO (t1u-t1g levels) appear as magnetically ordered with the positive X-ray polarization having lower electron yield current –we refer to this as negative dichroism, observed here in the absence of magnetic material. Conversely, the following peaks around 287.5 eV (LUMO+2,+3) have positive dichroism. In contrast to this spin polarization for π^* states, the σ^* antibond orbitals are weakly or not polarized, see figure 4. Similar results with a negatively polarized LUMO and positive higher π^* states can be obtained in samples with other Sc film thicknesses and under other experimental configurations (SI Appendix, section 4). The measurements show a time dependence due to charging effects and/or radiolysis, but the sign of the dichroism is changed when the Xray polarization is reversed or a negative magnetic field is applied.

There is a small peak some 5.5 eV above the LUMO, at 289.5 eV. This energy is too high for a charged LUMO π^* state. However, the resonance is too narrow and well defined for a σ^* state. Also, the peak becomes much stronger at low temperatures, indicating a quantum state difficult to observe at 300 K. We hypothesize that these characteristics may be interpreted as due to a delocalized superatom molecular orbital (SAMO), previously measured using low temperature scanning tunneling microscopy in C_{60} deposited on a metal surface.(53) The highest relative photo-ionization cross section would correspond to the s-wave orbital,(54) but here the energy gap to the LUMO is closer to values observed in microscopy for p- or d-wave orbitals. Another possibility is that this peak constitutes a carbon core exciton (CEx) close to the ionization potential.(55, 56) XMCD measurements show this state to have the same polarization direction as the LUMO. In addition to this prospective magnetically polarized SAMO, two non-polarized states become visible at low temperatures: the metal-coupled charged carbon state at 282-283 eV, and the peak due to aggregated or graphite-like C_{60} at 285.3 eV.

In conclusion, we have shown evidence for the universality of the emergent magnetism in metal-nanocarbon interfaces and its magnitude in different materials. Our results give evidence that it is indeed possible to have spin-polarized states at a metallic interface with molecular carbon even in the absence of magnetic materials. This is of critical importance in the design and measurement of organic spintronic devices and magnetic field sensors, where these interfaces can be used as spin filters. Furthermore, given changes in polarization at the different energy levels, a gate voltage may give us tuning access to spin up/down configurations or new quantum configurations, such as spin-polarized superatom orbitals or polarons. The possibility of tailoring the magnetic properties of transition metal-nanocarbon hybrids by using molecular interfaces opens as well tantalizing possibilities - for example in non-corrosive magnets, bio-compatible hybrid nanoparticles, metal recovery and in magnetic memories where the information is controlled via charge transfer with electro-optic irradiation.(5, 6)
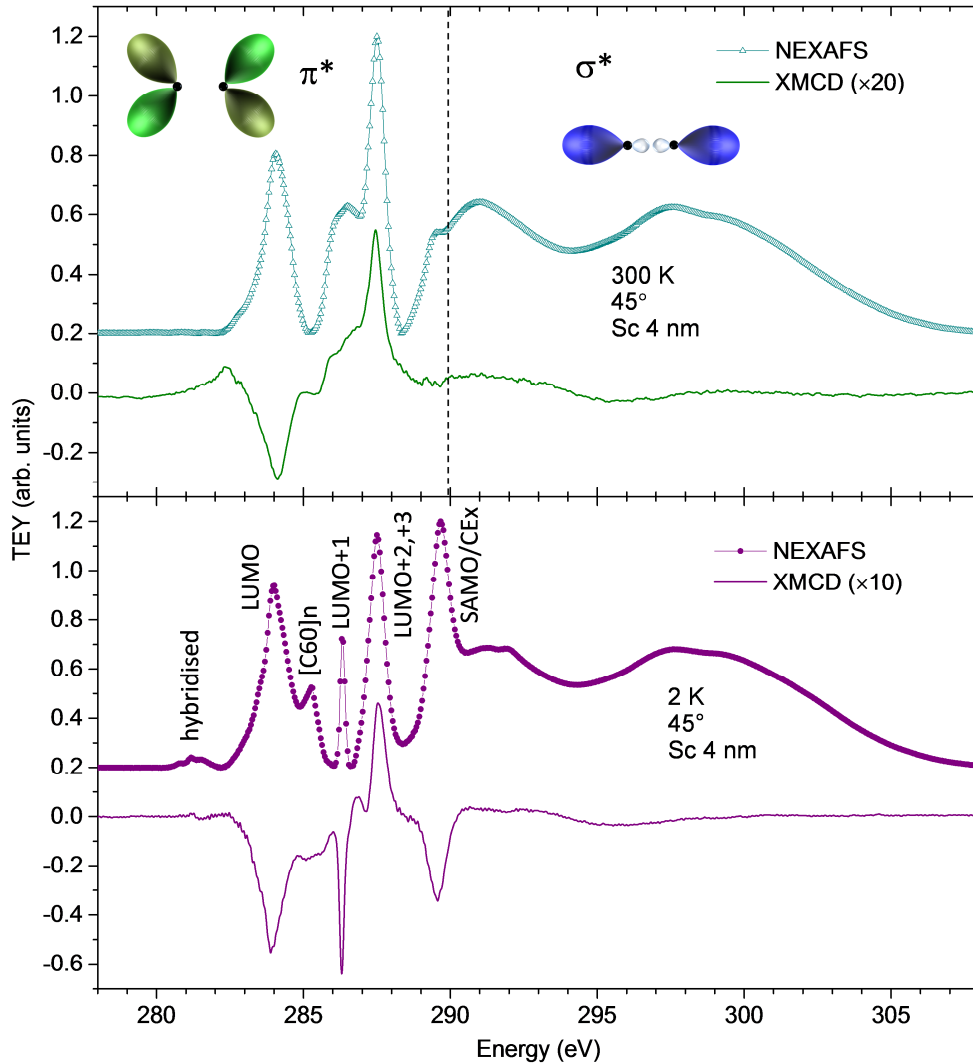
Figure 4: X-ray spectroscopy of C_{60} grown on a Sc 4 nm film collected at room temperature (top) and at 2 K (bottom). The measurements are done under an applied 1T perpendicular magnetic field in the total electron yield mode (TEY) and a 45º beam incidence. The NEXAFS show the typical structure of C_{60} −suggested modes in the bottom panel. Both measurements show magnetic dichroism, indicating the presence of a considerably large orbital polarization in the C_{60} density of states -even in the absence of a magnetic substrate. Note that XMCD measurements at low temperatures are multiplied by a smaller factor and that there is an additional, negatively polarized peak provisionally assigned to a superatom molecular orbital (SAMO) or core exciton (CEx).

1. Djeghloul F, *et al.* (2016) High Spin Polarization at Ferromagnetic Metal-Organic Interfaces: A Generic Property. *Journal of Physical Chemistry Letters* 7(13):2310-2315.
2. Barraud C, *et al.* (2010) Unravelling the role of the interface for spin injection into organic semiconductors. *Nature Physics* 6(8):615-620.
3. Raman KV, *et al.* (2013) Interface-engineered templates for molecular spin memory devices. *Nature* 493(7433):509-513.
4. Al Ma'Mari F, *et al.* (2015) Beating the Stoner criterion using molecular interfaces. *Nature* 524(7563):69-U128.
5. Atodiresei N & Raman KV (2014) Interface-assisted spintronics: Tailoring at the molecular scale. *Mrs Bulletin* 39(7):596-601.
6. Moodera JS, Koopmans B, & Oppeneer PM (2014) On the path toward organic spintronics. *Mrs Bulletin* 39(7):578-581.
7. Carmeli I, Leitus G, Naaman R, Reich S, & Vager Z (2003) Magnetism induced by the organization of self-assembled monolayers. *Journal of Chemical Physics* 118(23):10372-10375.
8. Vager Z & Naaman R (2004) Bosons as the origin for giant magnetic properties of organic monolayers. *Physical Review Letters* 92(8).
9. Naaman R & Vager Z (2010) Cooperative Electronic and Magnetic Properties of Self-Assembled Monolayers. *Mrs Bulletin* 35(6):429-434.
10. Crespo P, *et al.* (2004) Permanent magnetism, magnetic anisotropy, and hysteresis of thiol-capped gold nanoparticles. *Physical Review Letters* 93(8).
11. Hernando A, Crespo P, & Garcia MA (2006) Origin of orbital ferromagnetism and giant magnetic anisotropy at the nanoscale. *Physical Review Letters* 96(5).
12. Moorsom T, *et al.* (2014) Spin-polarized electron transfer in ferromagnet/C60 interfaces. *Physical Review B* 90(12).
13. Bairagi K, *et al.* (2015) Tuning the Magnetic Anisotropy at a Molecule-Metal Interface. *Physical Review Letters* 114(24).

14. Gruber M, *et al.* (2015) Exchange bias and room-temperature magnetic order in molecular layers. *Nature Materials* 14(10):981-+.

15. Raman KV & Moodera JS (2015) MATERIALS CHEMISTRY A magnetic facelift for non-magnetic metals. *Nature* 524(7563):42-43.

16. Cespedes O, Ferreira MS, Sanvito S, Kociak M, & Coey JMD (2004) Contact induced magnetism in carbon nanotubes. *Journal of Physics-Condensed Matter* 16(10):L155-L161.

17. Warner M, *et al.* (2013) Potential for spin-based information processing in a thin-film molecular semiconductor. *Nature* 503(7477):504-+.

18. Serri M, *et al.* (2014) High-temperature antiferromagnetism in molecular semiconductor thin films and nanostructures. *Nature Communications* 5.

19. Stoner EC (1938) Collective electron ferromagnetism. *Proceedings of the Royal Society of London Series a-Mathematical and Physical Sciences* 165(A922):0372-0414.

20. Janak JF (1977) UNIFORM SUSCEPTIBILITIES OF METALLIC ELEMENTS. *Physical Review B* 16(1):255-262.

21. Gruber M, *et al.* (2015) Spin-Dependent Hybridization between Molecule and Metal at Room Temperature through Inter layer Exchange Coupling. *Nano Letters* 15(12):7921-7926.

22. Stoner EC & Wohlfarth EP (1947) INTERPRETATION OF HIGH COERCIVITY IN FERROMAGNETIC MATERIALS. *Nature* 160(4071):650-651.

23. Stoner EC & Wohlfarth EP (1948) A MECHANISM OF MAGNETIC HYSTERESIS IN HETEROGENEOUS ALLOYS. *Philosophical Transactions of the Royal Society of London Series a-Mathematical and Physical Sciences* 240(826):599-642.

24. Candela GA & Haines RA (1979) METHOD FOR DETERMINING THE REGION OF SUPERPARAMAGNETISM. *Applied Physics Letters* 34(12):868-870.

25. Knobel M, *et al.* (2008) Superparamagnetism and other magnetic features in granular materials: A review on ideal and real systems. *Journal of Nanoscience and Nanotechnology* 8(6):2836-2857.

26. Schulz L, *et al.* (2011) Engineering spin propagation across a hybrid organic/inorganic interface using a polar layer. *Nature Materials* 10(1):39-44.

27. Morenzoni E, *et al.* (1994) GENERATION OF VERY SLOW POLARIZED POSITIVE MUONS. *Physical Review Letters* 72(17):2793-2796.

28. Morenzoni E, *et al.* (2002) Implantation studies of keV positive muons in thin metallic layers. *Nuclear Instruments & Methods in Physics Research Section B-Beam Interactions with Materials and Atoms* 192(3):254-266.

29. Prokscha T, *et al.* (2008) The new mu E4 beam at PSI: A hybrid-type large acceptance channel for the generation of a high intensity surface-muon beam. *Nuclear Instruments & Methods in Physics Research Section a-Accelerators Spectrometers Detectors and Associated Equipment* 595(2):317-331.

30. Yamamoto Y, *et al.* (2004) Direct observation of ferromagnetic spin polarization in gold nanoparticles. *Physical Review Letters* 93(11).

31. Niklasson AMN, Mirbt S, Skriver HL, & Johansson B (1997) Quantum-well-induced ferromagnetism in thin films. *Physical Review B* 56(6):3276-3280.

32. Cespedes O, Wheeler M, Moorsom T, & Viret M (2015) Unexpected Magnetic Properties of Gas-Stabilized Platinum Nanostructures in the Tunneling Regime. *Nano Letters* 15(1):45-50.

33. Hong SC, Lee JI, & Wu R (2007) Ferromagnetism in Pd thin films induced by quantum well states. *Physical Review B* 75(17).

34. Graf MJ*, et al.* (2003) Onset of antiferromagnetism in UPt3 via Th substitution studied by muon spin spectroscopy. *Physical Review B* 68(22).

35. Nakano T*, et al.* (2009) Fast muon spin relaxation in ferromagnetism of potassium clusters in zeolite A. *Physica B-Condensed Matter* 404(5-7):630-633.

36. Duty TL*, et al.* (1994) ZERO-FIELD MU-SR IN CRYSTALLINE C-60. *Hyperfine Interactions* 86(1-4):789-795.

37. Kiefl RF*, et al.* (1992) MOLECULAR-DYNAMICS OF THE MUONIUM-C60 RADICAL IN SOLID C-60. *Physical Review Letters* 68(17):2708-2712.

38. Filidou V*, et al.* (2013) Probing the C-60 triplet state coupling to nuclear spins inside and out. *Philosophical Transactions of the Royal Society a-Mathematical Physical and Engineering Sciences* 371(1998).

39. Prassides K*, et al.* (1992) MU-AT-THE-COST-OF-C70 - MONITORING THE DYNAMICS OF FULLERENES FROM INSIDE THE CAGE. *Journal of Physical Chemistry* 96(26):10600-10602.

40. Werner H*, et al.* (1994) REACTION OF MOLECULAR-OXYGEN WITH C-60 - SPECTROSCOPIC STUDIES. *Journal of the Chemical Society-Faraday Transactions* 90(3):403-409.

41. Ferrari AC & Robertson J (2004) Raman spectroscopy of amorphous, nanostructured, diamond-like carbon, and nanodiamond. *Philosophical Transactions of the Royal Society a-Mathematical Physical and Engineering Sciences* 362(1824):2477-2512.

42. Ferrari AC & Robertson J (2001) Resonant Raman spectroscopy of disordered, amorphous, and diamondlike carbon. *Physical Review B* 64(7).

43. Ferrari AC & Robertson J (2000) Interpretation of Raman spectra of disordered and amorphous carbon. *Physical Review B* 61(20):14095-14107.

44. del Corro E, Taravillo M, & Baonza VG (2012) Nonlinear strain effects in double-resonance Raman bands of graphite, graphene, and related materials. *Physical Review B* 85(3).

45. Lopez GA & Mittemeijer E (2004) The solubility of C in solid Cu. *Scripta Materialia* 51(1):1-5.

46. Barla A*, et al.* (2016) Design and performance of BOREAS, the beamline for resonant X-ray absorption and scattering experiments at the ALBA synchrotron light source. *Journal of Synchrotron Radiation* 23:1507-1517.

47. Ohldag H*, et al.* (2007) pi-Electron ferromagnetism in metal-free carbon probed by soft x-ray dichroism. *Physical Review Letters* 98(18).

48. Guo GY (1996) What does the K-edge x-ray magnetic circular dichroism spectrum tell us? *Journal of Physics-Condensed Matter* 8(49):L747-L752.

49. Shinohara H, Sato H, Saito Y, Tohji K, & Udagawa Y (1991) CARBON K-SHELL X-RAY ABSORPTION NEAR-EDGE STRUCTURE OF SOLID C-60. *Japanese Journal of Applied Physics Part 2-Letters* 30(5A):L848-L850.

50. Kondo D*, et al.* (2002) Unoccupied molecular orbitals of C-60 molecules adsorbed on Si(001)-(2 x 1) and Si(111)-(7 x 7) surfaces studied by NEXAFS. *Surface Science* 514(1-3):337-342.

51. Tran TLA*, et al.* (2011) Hybridization-induced oscillatory magnetic polarization of C-60 orbitals at the C-60/Fe(001) interface. *Applied Physics Letters* 98(22).

52. Wong PKJ*, et al.* (2013) Electronic and magnetic structure of C-60/Fe3O4(001): a hybrid interface for organic spintronics. *Journal of Materials Chemistry C* 1(6):1197-1202.

53. Feng M, Zhao J, & Petek H (2008) Atomlike, hollow-core-bound molecular orbitals of C-60. *Science* 320(5874):359-362.

54. Bohl E*, et al.* (2015) Relative Photoionization Cross Sections of Super-Atom Molecular Orbitals (SAMOs) in C-60. *Journal of Physical Chemistry A* 119(47):11504-11508.

55. Ma Y *, et al.* (1993) CORE EXCITONS AND VIBRONIC COUPLING IN DIAMOND AND GRAPHITE. *Physical Review Letters* 71(22):3725-3728.

56. Saito Y, Shinohara H, & Ohshita A (1991) ELECTRON-ENERGY LOSS SPECTRUM NEAR CARBON K-EDGE IN SOLID C-60. *Japanese Journal of Applied Physics Part 2-Letters* 30(6B):L1145-L1147.

57. Associated data to this manuscript can be found at http://doi.org/10.5518/179

Supplementary Information for Emergent Magnetism at Transition Metal-Nanocarbon Interfaces

S.1 Sample growth and magnetometry:

All thin films were deposited onto Si/SiO$_2$ substrates. Thin films of C$_{60}$ were deposited by sublimation in a dual evaporation-sputter deposition system under high vacuum (on the order of 10^{-8} Torr). The C$_{60}$ is deposited via high vacuum thermal sublimation at rates of 0.5-1 Å/s. The molecules were from a source of 99.9% purity bought from Sigma-Aldrich. Thin metallic films of scandium (99.9% purity), copper (99.999% purity) and platinum (99.9% purity) were deposited at ambient temperature using DC magnetron sputtering with a 24 sccm argon gas flow at a sputtering pressure of 2.5 mtorr (10^{-8} torr base pressure) with a deposition rate of 1-3 Å/s. An aluminum cap of 3-10 nm was deposited on top of the devices to prevent oxidation of the sample. The metallic films are continuous and there is no evidence for significant interdiffusion as seen in low angle Xrays and Raman spectroscopy. Xray absorption spectroscopy spectra of our samples do not show impurities.
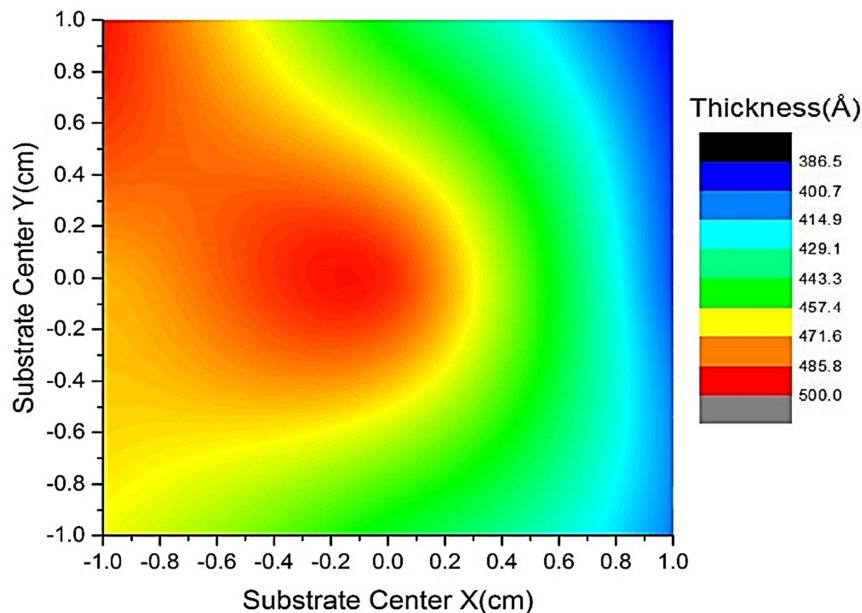

Figure S1: C$_{60}$ film thickness uniformity over a 2×2 cm^2 surface, similar to those used for low energy muon spin spectroscopy. Magnetometry, Raman and XMCD are measured on samples of 0.5×0.5 cm^2 or smaller.

The magnetometry results were taken using a MPMS3 superconducting quantum interference device operated as a vibrating sample magnetometer (SQUID-VSM or SVSM) from Quantum Design. The instrument has a resolution limit better than 10^{-8} emu, and the typical moment for our samples varies between ~10^{-7} (background signal of the silicon substrate and holder) to 10^{-5} emu (strong and/or multi-layered Cu-nanocarbon samples).

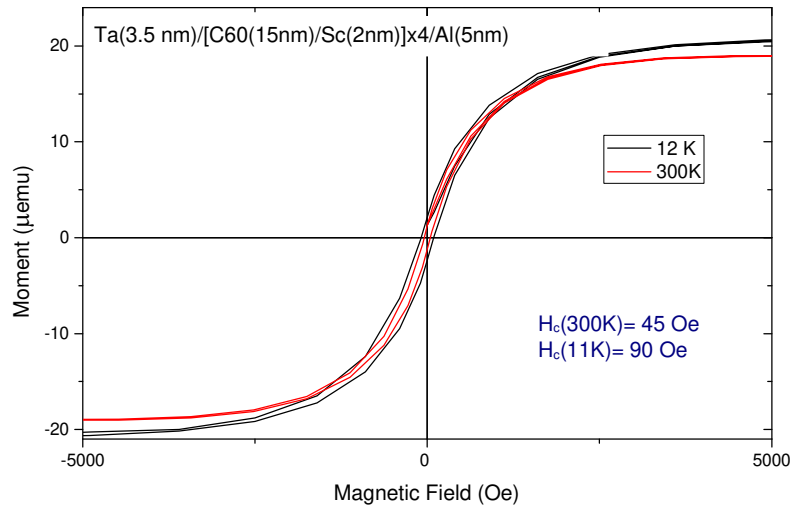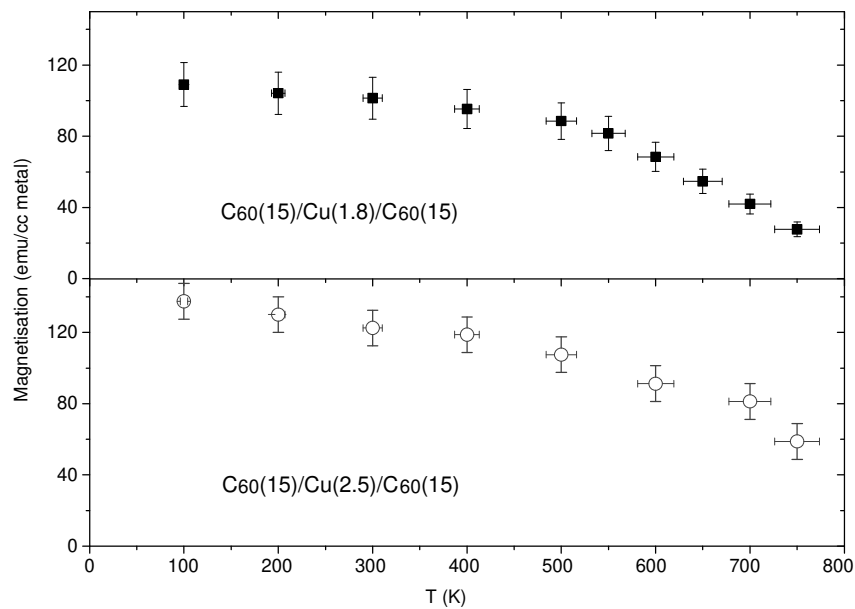*Figure S2: Typical hysteresis loops at 300 K and 12 K for a Sc/C_{60} multilayer.*

Figure S3: Magnetisation v temperature for $C_{60}(15)$/Cu(x)/$C_{60}(15)$ trilayers with x=1.8 nm (top) and 2.5 nm (bottom). Each data point corresponds to a hysteresis loop corrected for linear background contributions.

In SQUID magnetometry, the moment increases with the number of interfaces and therefore depositing several multilayers improves the signal to noise ratio as well as reducing the sample to sample variation (several interfaces automatically averaged within a single sample). On the other hand, adding more layers leads to enhanced roughness, which reduces the relative contribution of the top layers –but only if the total thickness of the sample is also increased. Otherwise, if the total thickness is maintained and the number of interfaces increased, the roughness is reduced and not increased, see figure 1b. We also need to take into account that the degradation rates and recovery under annealing are affected by the number of layers, with the top layers being less magnetic but acting as effective caps that preserve the magnetism of the bottom layers when needed over long time periods for extensive measurements. Therefore, different samples structures are measured to reach the optimal values over the time of the measurements.
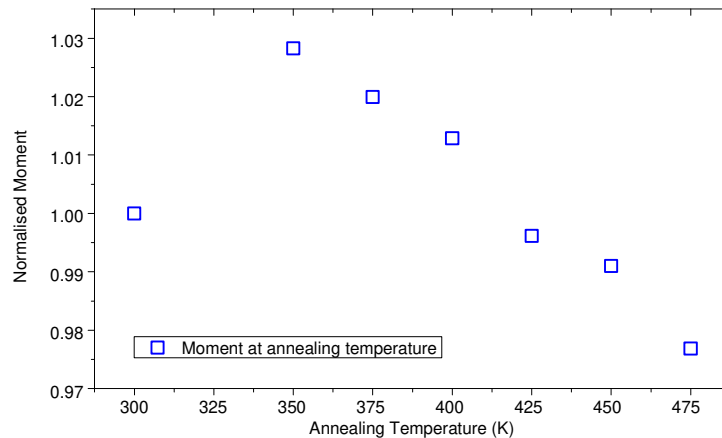
Figure S4: Changes during annealing in the magnetization of a Sc/C60 multilayer with the structure Si//Ta(3.5nm)/ [C60(15nm)/Sc(1.5nm)]x4 /Al(5nm). Although the trend is similar, note that changes at 350-475 K (±3%) are much smaller than the 15% enhancement observed in a single trilayer C60(20)/Sc(1)/C60(20), see figure 3B in the manuscript. This is due to the reduced degradation and de-oxygenation in a sample with thicker scandium and several metal layers.

S2. Density functional theory (DFT) simulations:

Standard and fixed spin-moment(S1), van der Waals (vdW) corrected(S2), Density Functional Theory (DFT) simulations were executed via the Projected Augmented Wave (PAW) method as implemented in the VASP program(S3) with the PBE exchange-correlation (XC) functional,(S4) a 400 eV plane-wave energy cut-off, (0.2 eV, 1st order) Methfessel-Paxton electronic smearing,(S5) and a 10 symmetry irreducible k-point grid. The atomic-force threshold for geometry optimization was 0.02 eV Å^{-1}. In all cases, a vacuum separation of at least 12 Å was present between replicated images of the interface models. To facilitate comparison between the results for the C_{60}/Cu and aC/Cu interfaces, the Cu substrate was consistently modelled as the 7-vacancy Cu(111)-4x4 reconstruction(S6, S7).

The models for the C_{60}/Cu interface were the same C_{60}/7-vacancy Cu(111)-4x4 systems as in Ref. (S8). The aC models were initially prepared by creating random samples of different densities (1.4, 1.7, 2.3 and 2.6 gr/cc) at a distance of 1.5 Å above a 7-vacancy Cu(111)-4x4 slab of three Cu layers. Five different random systems for each density were created and each of them was optimized together with the Cu-susbstrate. The lowest energy aC/Cu structure for each aC density was used to prepare the initial geometries for the systems with more Cu layers, adding extra Cu(111) layers (up to overall ten Cu layers). The structure of these systems was eventually optimized relaxing all the C atoms and the five topmost Cu layers. Figure S5 shows the optimized structure for the considered aC/Cu(111)-4x4 slabs (3 Cu layers).
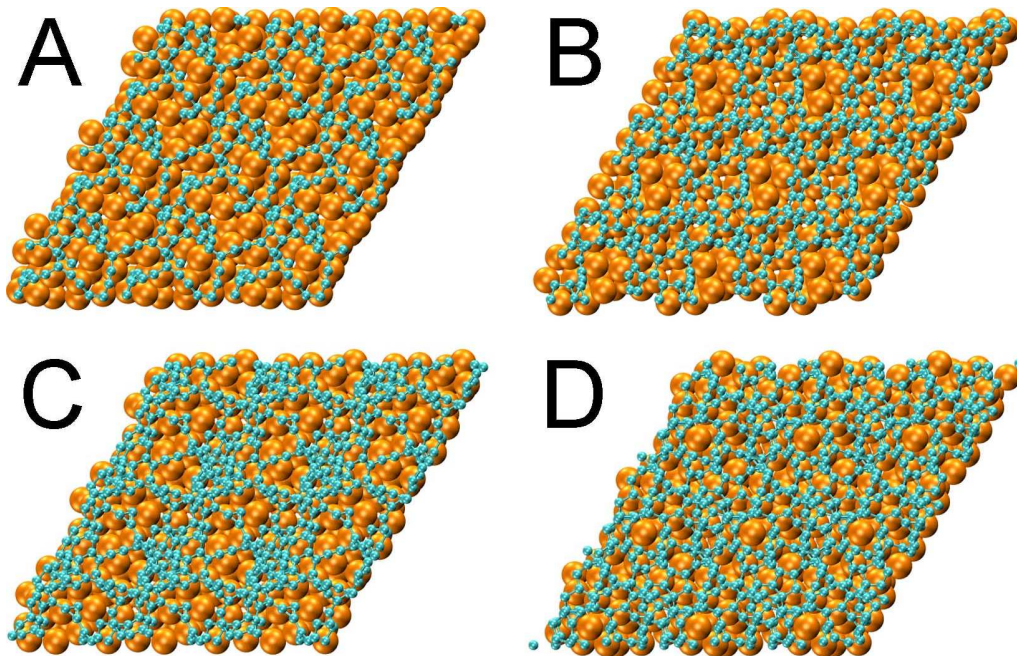

Figure S5: Optimized atomic structure for the considered aC(pale blue)/Cu(orange) models on the 3 Cu-layer slabs. (A) 1.4 gr/cc, (B) 1.7 gr/cc, (C) 2.3 gr/cc, (D) 2.6 gr/cc. C: blue, Cu: orange.

Due to the modelled non-magnetic ground-state for all the C_{60}/Cu and aC/Cu models, atom-resolved approximations to Stoner exchange integrals (I_s) were computed by enforcing a magnetic moment of 0.075 μ_B/Cu atom via fixed spin-moment DFT. Following (S9) and (S8), atom-resolved values of I_s were computed from the (PAW-core projected) band-splitting at the Fermi energy [$\Delta\epsilon(E_F)$] and the (PAW-core projected) atomic magnetic moment (Δm) as:

[1] $\qquad I_S = -\dfrac{\Delta\epsilon(E_F)}{\Delta m}$

As shown in Figure S6, the simulations suggest that the contribution to the total magnetic moment (M_{tot}) due to the interface region (M_{int}), arbitrarily defined as the carbon layer and the five topmost Cu layers, is larger for the denser (≥ 2.3 gr/cc) aC films than for the C_{60} one. The simulation indicate that, as the thickness of the Cu slab increases, M_{int} for the C_{60}/Cu system is more strongly quenched than for the aC/Cu models. This result is in line with the measured weaker dependence on the Cu-film thickness of the interface magnetization of aC samples with respect to C_{60} ones [Fig. 1 and (S8)], suggesting a stronger (weaker) coupling of the interface magnetization with bulk-like metallic states in the Cu-sample for the C_{60} (aC) films.
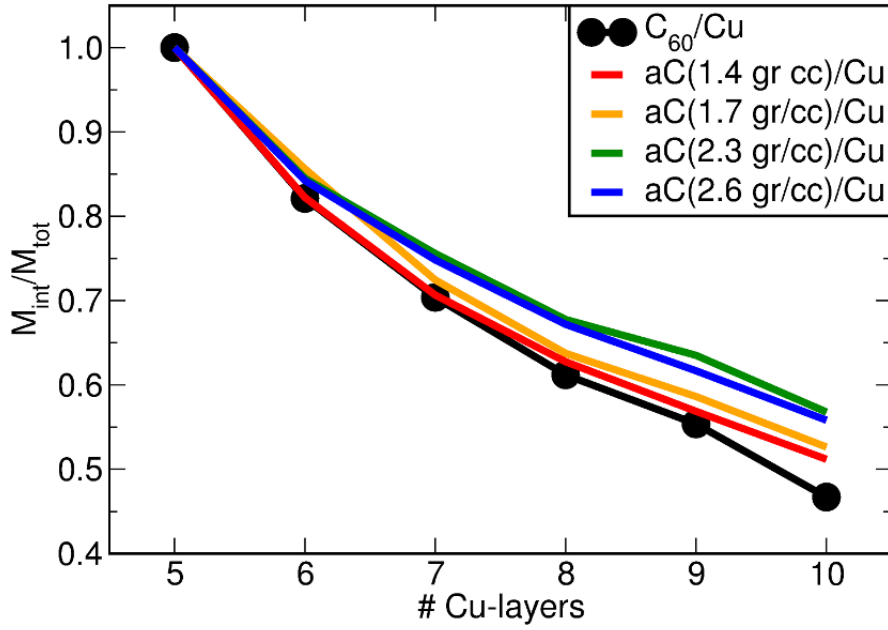

Figure S6: Calculated ratio between the interface (M_{int}) and total magnetic moment (M_{tot}) of the C_{60}/Cu and aC/Cu models as a function of the carbon-film and thickness of the Cu-slab. The computed interface contribution is larger for the denser (≥ 2.3 gr/cc) aC films. The interface region has been arbitrarily defined as the carbon layer and the five topmost Cu layers.

Further support of the effect of the nature of the carbon-layer on the coupling between the innermost part of the Cu film and the interface region is provided by atom-resolved analysis of the Stoner exchange integral (I_S) as a function of the distance from the carbon-Cu interface (Figure S7). Whereas for the C_{60}/Cu model enhancement of I_s with respect to the bulk value (*magnetic hardening*) is found also for Cu atoms at large distances from the most intimate C-Cu interface, in the case of the aC films the magnetic hardening is concentrated close to the carbon substrate, leading to larger accumulation of the magnetic moment at the interface region for aC films with respect to C_{60} ones (Fig. S6), and the observed weaker dependence of the magnetic signals on the metal-sample thickness for aC films (Figure 1).
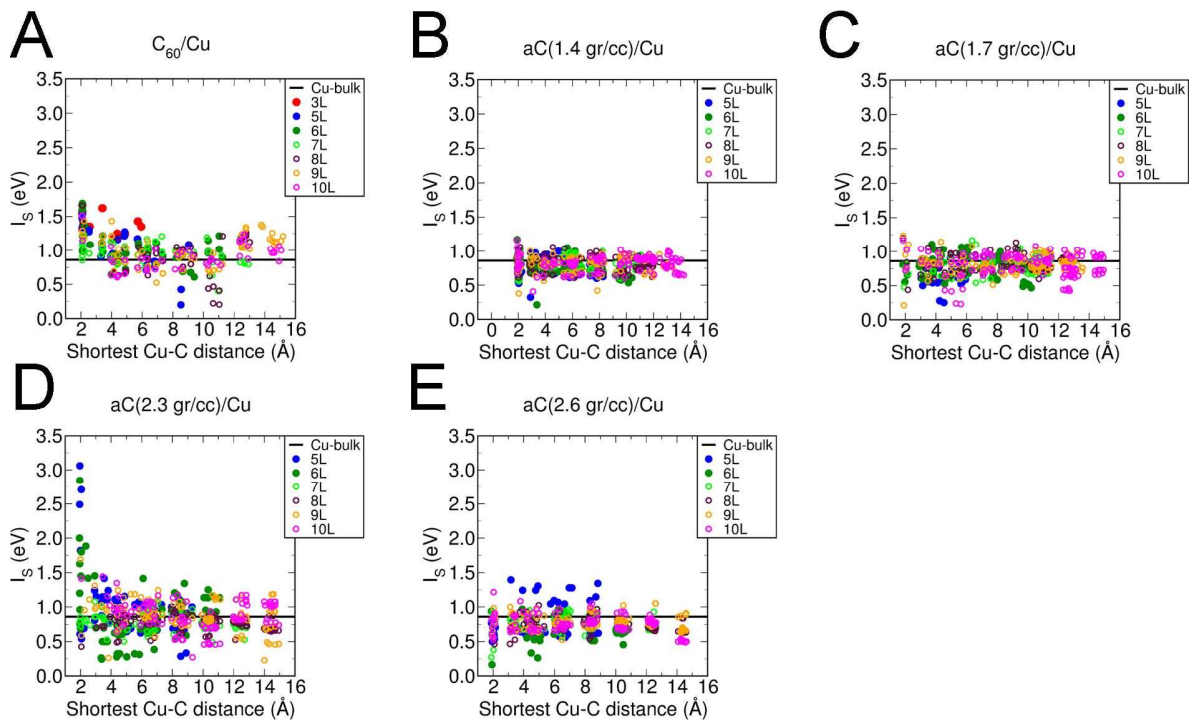

Figure S7: Atom-resolved analysis of the Stoner exchange integral (I_s) for the Cu-atoms of the considered C_{60}/Cu (A) and aC/Cu (B)-(E) interface models as a function of their shortest distance from the C atoms.

S.3 Low energy muon spin spectroscopy:

Low energy muon spin spectroscopy is used to probe the local magnetisation in our multi-layered structures. In this technique, anti-muons are implanted into a sample at different energies and therefore at different depths from the surface. Once stopped, the particles decay into a detectable positron and a neutrino/anti-neutrino pair. The method uses the preferred handedness of particles and anti-particles implicit in CP violation to provide a probe of local magnetization. The restriction that the emitted positron must be right-handed results in a preferred direction of emission along the direction of the μ^+ spin vector. Determining the direction of the positron decay allows the precession of the anti-muon spin to be observed and, therefore, the local field at the anti-muon implantation site to be determined. A polarized beam of high energy (about 4 MeV) anti-muons is obtained from the decay of π+ generated in collisions of the 590 MeV proton beam of the PSI cyclotron with carbon nuclei of a graphite target. A high intensity beam of these energetic muons is sent onto a cryogenic moderator consisting of a 300-nm-thin solid argon layer deposited on a 10 K cold silver foil. Moderated muons with a mean energy of about 15 eV are re-accelerated electrostatically to keV energies, forming the low-energy muon beam with tuneable implantation energy. A spin rotator, made of a crossed electric and magnetic field, was used to set an angle of 10° between the sample plane and the anti-muon beam polarization. Of the implanted anti-muons, some 20% were expected to form muonium when stopped in the C_{60} layers. Positrons emitted from muon decay were captured by two sets of detector segments, forward and backward, and the count difference between these two detector sets was used to determine the spin direction of implanted anti-muons as a function of time.
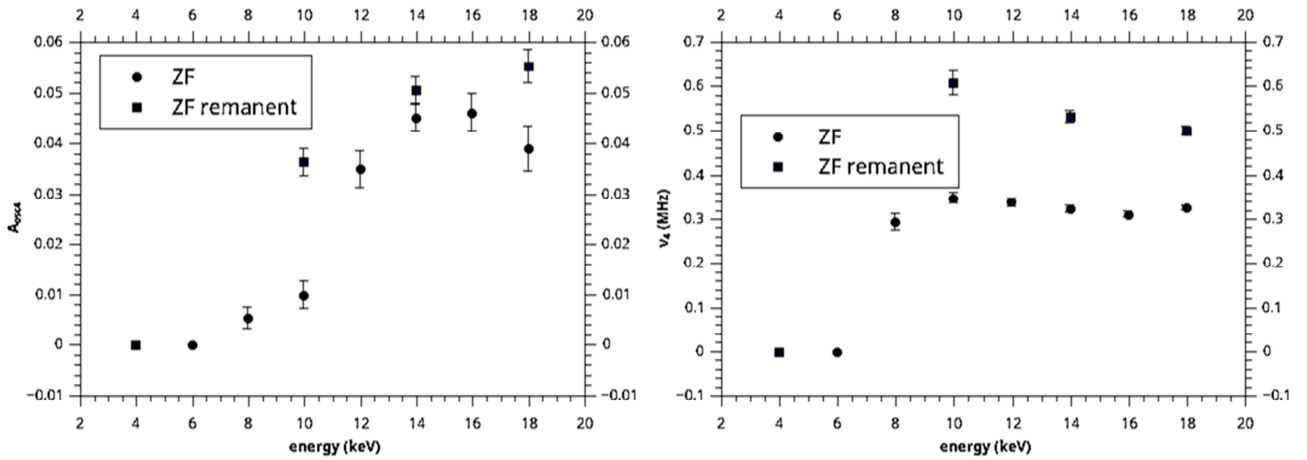
Figure S8: Left: Muon oscillation amplitude at zero field and remanence for Si//Ta(3)/C$_{60}$(25)/Cu(2.5)/C$_{60}$(50)/Cu(15)/C$_{60}$(25)/Au(25). Right: Frequencies for the oscillation. Below 8 keV, the muons can only penetrate to the top Au/C$_{60}$ layers, where this slow oscillation is not present or easily observed (see penetration profiles for this sample in figure 2 of the main manuscript).

The objective was partly to use the depth profile of the particles to assess the relative contributions of two metal layers (4 interfaces) with different thicknesses. The measurement points to an enhanced signal in thinner layers, i.e. the stronger signal in thinner films is not simply due to equal magnetic moments in a smaller volume, but may have other contributions such as interface-to-interface coupling or reduced screening when the metal layer is sufficiently thin.

S.4 Raman spectroscopy:

Raman spectra were measured using a LabRAM HR800 from Horiba Sci. with a 532 nm excitation laser and a 600 ln/mm grating to obtain a resolution of the order of 1 cm^{-1}. Changes in the Raman spectra can be used to determine the carbon structure and hybridisation. In as-deposited films, the carbon G peak position is found at ~1530 cm-1, which is in good agreement with values previously found in amorphous carbon. As the film is annealed, the carbon atoms rearrange and form graphitic nanocrystals. Once the carbon film is fully composed of these nanocrystals, the G peak should be found at 1600 cm^{-1} with benzene-like ring arrangements. In our case, the G peak reaches a maximum value of 1615 cm^{-1}, close to but not identical to the ideal value of 1600 cm^{-1}. This is indicative of the presence of small amounts of sp2 chains that can originate due to the growth of tetrahedral amorphous carbon (ta-C) and/or in the presence of hydrogen during deposition –please see the seminal work by Ferrari and Robertson (refs. 41-43 in the main manuscript). Annealing at higher temperatures lead to a reduction in the G peak frequency, which may be related to the conversion of these chains in to benzene ring arrangements and/or the formation of graphite and inter-sheet bonding. Pure graphite has a G peak position of 1580 cm^{-1}, and therefore requires annealing temperatures above 1000 K. These values may be different for sputtered carbon on other substrates.
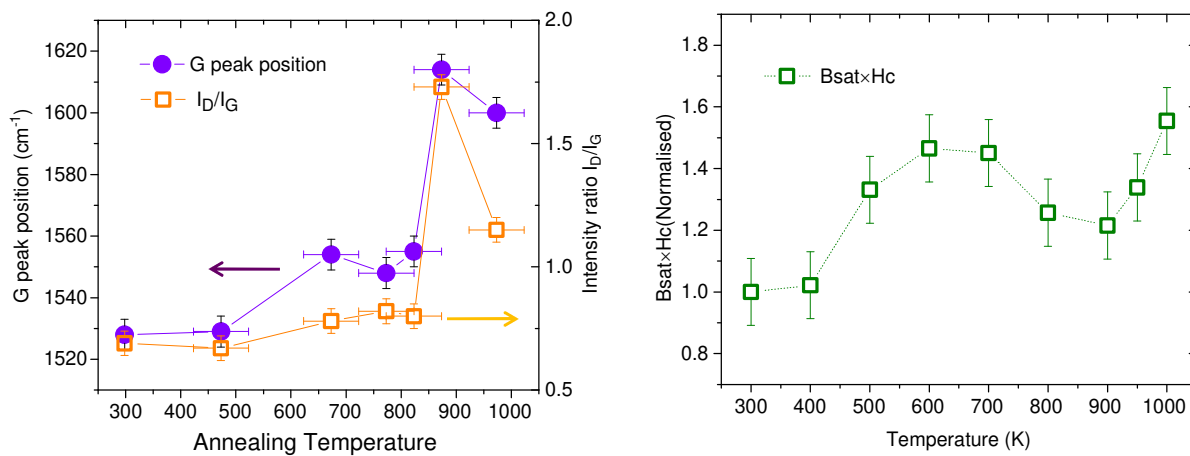

Figure S9: Left: changes with annealing temperature in the position of the carbon G peak and the D to G peaks Raman intensity ratio (ID/IG), and Right: the magnetic strength (Bsat×Hc product) for two copper-sputtered carbon interfaces annealed in-situ (magnetometry) and ex-situ (Raman). The sp3 → sp2 conversion is expected to be completed at 850-900 K.

S.5 X-ray absorption spectroscopy:

X-ray Absorption Spectroscopy (XAS) using X-ray Magnetic Circular Dichroism (XMCD) was performed in the BOREAS beamline of the ALBA Sychrotron. Details of design and performance of the beamline can be found in Barla, A., Nicolás, J., Cocco, D., Valvidares, S.M., et al., J. Synchrotron Rad. 23(6), 1507-1517 (2016).
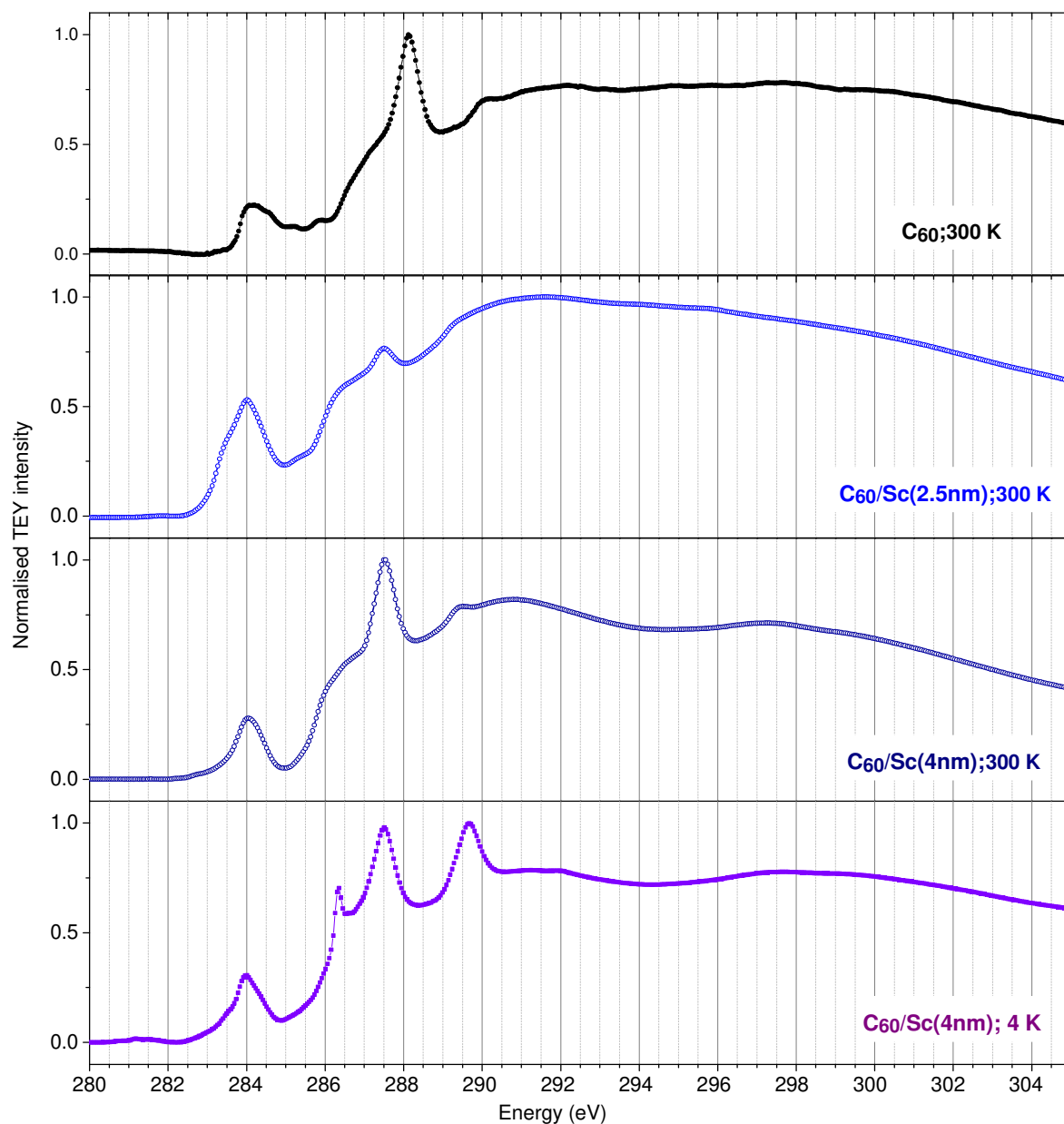

Figure S10: Raw XAS spectra before edge correction for C_{60} on a Si substrate (top) and C_{60} layers on Sc films of 2 and 4 nm at 300 and 4 K. The bottom two panels are the spectra for the results in figure 4 of the main manuscript before edge correction.

In measurements of the carbon K-edge, electrons are excited from the core $1s$ level to the p valence shell. The photon spin is transferred to the photoelectron as an angular momentum, so the dichroism can only be detected if the p shell possesses an orbital moment itself. Sensitivity to the spin magnetic moment of the p shell arises only indirectly through the spin-orbit interaction (see Magnetism: From Fundamentals to Nanoscale Dynamics by J. Stöhr and H.C. Siegmann). The C_{60} may undergo changes in its edge structure during the measurement due to charging effects and/or radiolysis. In XMCD, these effects are accounted for by averaging over time measurements with different circular polarisations and by measuring under different conditions. In XMCD, due to the short scape distance of the emitted electrons, we only probe the top 1-5 nm of the sample, and therefore a single interface is only probed.
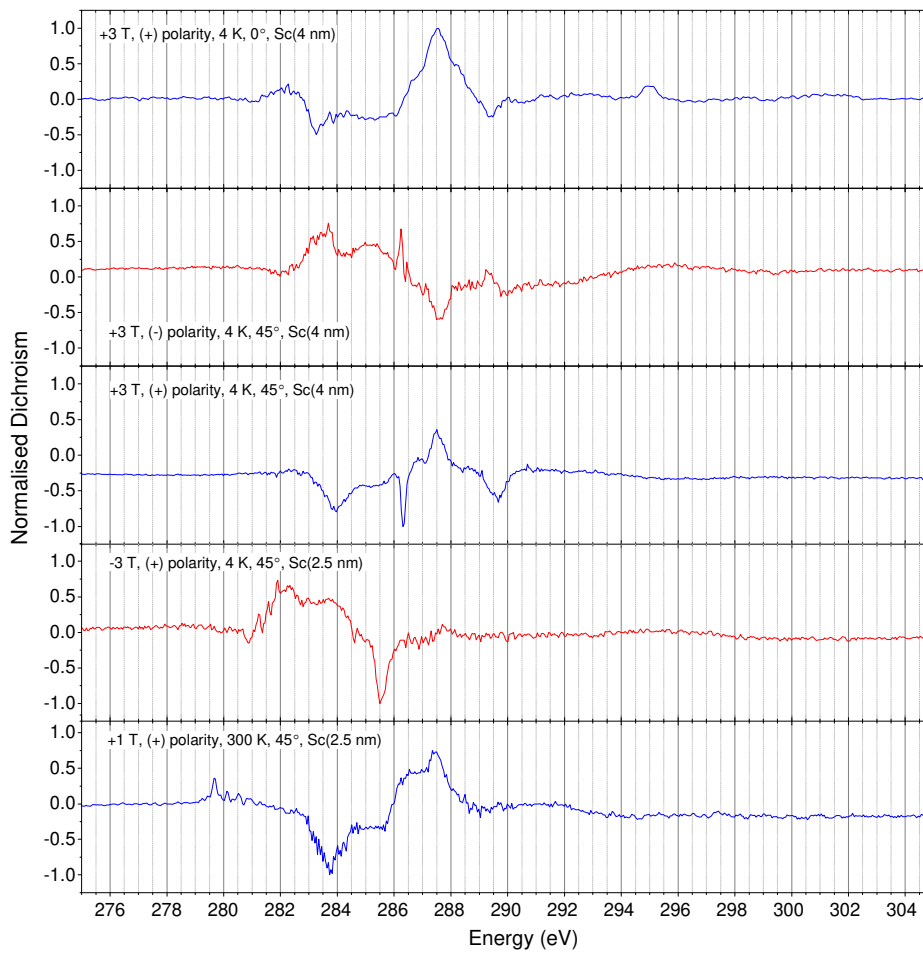

Figure S11: Examples of XMCD at the carbon K-edge measured in two samples with different Sc film thickness and under different conditions. Angles refer to the orientation of the film plane respect to the magnetic field axis. Measurements plotted in red are taken in a negative magnetic field or with a reversed polarisation; starting the measurement with the light polarisation vector antiparallel to the magnetic field and subtracting the electron yield parallel to the field. A Fe ferromagnetic film for positive applied field and light polarisation axis parallel to the field shows positive XMCD at L3.

S1. Djeghloul F, *et al.* (2016) High Spin Polarization at Ferromagnetic Metal-Organic Interfaces: A Generic Property. *Journal of Physical Chemistry Letters* 7(13):2310-2315.

S2. S. Grimme, J. Antony, S. Ehrlich, and S. Krieg, ``A consistent and accurate ab initio parametrization of density functional dispersion correction (dft-d) for the 94 elements H-Pu'', J. Chem. Phys. **132**, 154104 (2010).

S3. Kresse, G. & Furthmuller, J. Efficient iterative schemes for ab initio total-energy calculations using a plane-wave basis set. *Physical Review B* **54**, 11169-11186 (1996).

S4. Perdew, J. P., Burke, K. & Ernzerhof, M. Generalized gradient approximation made simple. *Physical Review Letters* **77**, 3865-3868 (1996).

S5. Methfessel, M. & Paxton, A. T. HIGH-PRECISION SAMPLING FOR BRILLOUIN-ZONE INTEGRATION IN METALS. *Physical Review B* **40**, 3616-3621 (1989).

S6. Pai, W. W. *et al.* Optimal Electron Doping of a C-60 Monolayer on Cu(111) via Interface Reconstruction. *Physical Review Letters* **104**, 036103 (2010).

S7. Xu, G. *et al.* Detailed low-energy electron diffraction analysis of the (4 x 4) surface structure of C-60 on Cu(111): Seven-atom-vacancy reconstruction. *Physical Review B* **86**, 075419 (2012).

S8. Al Ma'Mari F, *et al.* (2015) Beating the Stoner criterion using molecular interfaces. *Nature* 524(7563):69-U128.

S9. O. Gunnarsson, *J. Phys. F: Metal Phys.* **6**, 587 (1976).